J Mater Sci (2017) 52:9819–9833

Metals

The grain boundary character distribution of highly twinned nanocrystalline thin film aluminum compared to bulk microcrystalline aluminum

Gregory S. Rohrer[1], Xuan Liu[2], Jiaxing Liu[2], Amith Darbal[2], Madeleine N. Kelly[1], Xiwen Chen[3], Michael A. Berkson[3], Noel T. Nuhfer[1], Kevin R. Coffey[4], and Katayun Barmak[3,*]

[1] *Department of Materials Science and Engineering, Carnegie Mellon University, 5000 Forbes Avenue, Pittsburgh, PA 15213, USA*
[2] *NanoMEGAS USA, 1095 W. Rio Salado Parkway #110, Tempe, AZ 85281, USA*
[3] *Department of Applied Physics and Applied Mathematics, Columbia University, 500 W. 120th St., New York, NY 10027, USA*
[4] *Department of Materials Science and Engineering, University of Central Florida, 4000 Central Florida Boulevard, Orlando, FL 32816, USA*

Received: 25 February 2017
Accepted: 18 April 2017
Published online: 24 April 2017

ABSTRACT

The grain boundary character distribution (GBCD) of a 100-nm-thick Al thin film was measured as a function of annealing time by transmission electron microscopy-based crystal orientation mapping and compared to a bulk material with a grain size of 23 μm. The most significant difference between the thin film and bulk GBCDs is the concentration of Σ3 boundaries (boundaries with a misorientation of 60° around [111]), which were mostly coherent twins. The length fraction of Σ3 boundaries in the as-deposited thin film is 0.245, more than ten times the length fraction in the bulk sample (0.016). Although the concentrations of Σ3 boundaries are very different in the two samples, the population distributions are strongly correlated for all misorientations except Σ3. The results indicate that the characteristic GBCD develops at grain sizes as small as 109 nm. Annealing the thin film samples at 400 °C for 30 min or more leads to a strong ⟨111⟩ grain orientation texture and a decrease in the concentration of Σ3 grain boundaries. Grain size distributions for the samples in the current study show good agreement with prior reports that used image-based methods.

Introduction

The properties of materials are strongly influenced by the types of grain boundaries in the material and how they are connected [1–5]. Using scanning electron microscopy (SEM)-based electron backscatter diffraction (EBSD) [6], it has been possible to measure the relative areas of different types of grain boundaries over all five independent crystallographic parameters [7–10]. This quantity is referred to as the grain boundary

Address correspondence to E-mail: kb2612@columbia.edu

DOI 10.1007/s10853-017-1112-8

character distribution (GBCD) and is parameterized in terms of the lattice misorientation and the grain boundary plane normal [11].

The GBCDs of many materials with grain sizes in the micrometer range have been measured using the SEM-based technique [7–10, 12–15]. The results from materials with micrometer-scale grain sizes produced by grain growth are all consistent with the conclusion that the relative populations of grain boundaries scale inversely with the grain boundary energies [16]. Studies of the same materials with different grain sizes suggest that this distribution is independent of grain size [17]. So, the question arises, at what point in microstructure development does the distribution arise? The main limitation in trying to answer this question is that the SEM-based orientation mapping does not have the spatial resolution to characterize the shapes of grain boundaries in nanocrystalline materials. With the emergence of a high-speed transmission electron microscopy (TEM) nanodiffraction-based orientation mapping technique [18–21], it has been possible to quantitatively evaluate the GBCD of nanocrystalline materials [22–28]. The ability to map orientations with a nm-scale resolution makes it possible to measure the GBCDs of nanocrystalline materials and compare them to those of microcrystalline materials. For simplicity, throughout the remainder of the text and in the title, materials with grain sizes in the micrometer range are termed microcrystalline and those with grain sizes in the nanometer range are termed nanocrystalline.

In one previous study, Liu et al. [25] measured the GBCD of a nanocrystalline tungsten film and compared it to that of a microcrystalline Fe sample, which also has body-centered cubic (BCC) structure. The correlation between the two GBCDs suggests a similarity between nanocrystalline and microcrystalline interfacial structures. Furthermore, the GBCDs of thin film nanocrystalline Cu [23, 24, 27] are consistent with bulk Cu [29]. More recently, the GBCD of an electrodeposited Cu film with micrometer-scale grains and much smaller twins was measured by EBSD and found to be similar to the GBCD of bulk Cu [30]. Here we extend the previous studies by measuring and comparing the GBCDs of thin film and bulk Al samples that have a face-centered cubic (FCC) crystal structure and grain sizes that differ by a factor of more than 200. In this case, the nanocrystalline samples are physical vapor-deposited thin films in the as-deposited state and after annealing at 400 °C. It should be noted that the structure of the thin film might impose geometric constraints on the GBCD. For example, if there is strong texture and the film is columnar, then this will constrain the types of grain boundaries that can form.

The purpose of this paper is to compare the GBCDs of an Al thin film at different stages of annealing and with grain sizes on the order of 100 nm to a bulk sample of Al with a grain size more than 200 times larger. In the results section, it is shown that the most significant difference between the GBCDs of the thin film and bulk samples is the population of Σ3 grain boundaries, indicating that characteristic and anisotropic GBCDs can be obtained even at grain sizes on the order of 100 nm. Annealing the as-deposited microstructure leads to grain growth, a strong ⟨111⟩ grain orientation texture, and a decrease in the population of Σ3 grain boundaries.

Materials and methods

The aluminum film examined in this work has a nominal thickness of 100 nm, similar to films we have studied previously [31]. It was sputter deposited from a 99.99% pure Al target onto an oxidized Si (100) wafer with a 300-nm-thick thermal oxide layer. The base pressure of the chamber was in the 10^{-8} Torr range prior to deposition. The sputtering gas was ultrahigh purity 99.9995% Ar at a pressure of 3 mTorr and a flow rate of 20 sccm. The substrate was rotated at 10–15 rpm to ensure good thickness uniformity. The substrates were nominally at room temperature (no intentional heating). Following deposition, the substrate was cleaved into smaller pieces. These pieces were then encapsulated in borosilicate glass tubes that were evacuated to the 10^{-6}–10^{-7} Torr range prior to being sealed. The samples in the sealed tubes were annealed at 400°C for 30 or 150 min. This paper will compare the microstructure of the as-deposited sample with the annealed samples.

The plan-view TEM samples were prepared by first removing most of the Si substrate by mechanical polishing from the back side and then removing the rest by chemical etching using a mixture of HF and HNO_3 [32]. The etching was stopped in the oxide layer before breaking into the Al film, resulting in large, uniformly thick, electron transparent samples for plan-view TEM. All of the orientation maps were recorded using an ASTAR™ (NanoMEGAS, Brussels, Belgium)

orientation mapping system installed on a Philips CM 200 TEM with a field emission gun and an accelerating voltage of 200 kV. A 20-μm second condenser aperture was used for the mapping, and the diffraction patterns were recorded with a precession angle of 0.6°. Diffraction patterns, from which the orientation maps were derived, were collected at intervals (i.e., step sizes) of 4 nm for the as-deposited film and 5 nm for the two annealed films. The orientation maps were analyzed using the TSL OIM^{TM} software (EDAX, Mahwah, NJ, USA) after adjusting for the reference frame difference between the ASTAR^{TM} and TSL systems, as described in detail elsewhere [24].

The orientation data were subjected to a cleanup procedure to eliminate unindexed and incorrectly indexed points. First, the grain dilation filter was used with a minimum grain size of 7 pixels and a tolerance angle of 5°. In previous work by Liu et al. [28], the procedure for determination of the minimum grain size value in the grain dilation filter is described in more detail. Next, a single, averaged orientation was assigned to all of the pixels within a grain, assuming all adjacent pixels with disorientations ‹5° belonged to the same grain. And finally, for the GBCD determination, grain confidence index standardization was used to assign the same confidence index to each pixel within a grain. Throughout this paper, when the term disorientation is used, it indicates the minimum misorientation.

A sample orientation map of the as-deposited Al film after cleanup is shown in Fig. 1a. In Fig. 1b, grain boundary line segments determined from the orientation maps are illustrated. Grain boundary traces were reconstructed with a grain tolerance of 2 pixels such that the line segments deviate from the true boundary positions by no more than two pixels. All boundaries within 5° of the Σ3 misorientation, 60° around the [111] axis, are colored blue [33]. Those Σ3 boundaries with line segments that are less than 5° from the (111) plane trace in both grains are assumed to be coherent twin boundaries and are colored red. The boundary map in Fig. 1b reveals that multiple grains have an internal, finely structured network of apparent boundaries that are likely caused by the "pseudo-symmetry" problem. These pseudo-symmetry boundaries are created within single grains where diffraction patterns can be indexed in multiple orientations related by simple symmetry operations.

For grain size determination, the pseudo-symmetry boundaries were removed using the TSL OIM^{TM} software following the procedure detailed by Liu et al. [28], with one exception. The Σ3 boundaries were not removed in the current work, given that they are present in very significant fractions. The reconstructed grain boundary maps were used to obtain the grain areas using ImageJ in the manner of our previous work. [31] The edge grains were excluded from the data set. The grain areas were then used to determine three linear measures of grain size: (i) equivalent circle diameter of mean area, $d_{\langle A\rangle} = \sqrt{\frac{4\langle A\rangle}{\pi}}$, where $\langle A\rangle$ is the mean value of grain areas, and (ii) and (iii) the mean and median equivalent circle diameters, $\langle D\rangle$ and D_{med}, by first determining the equivalent circle diameter for each grain in the data set, namely $D = \sqrt{\frac{4A}{\pi}}$, and then determining the mean and median of these diameters. All

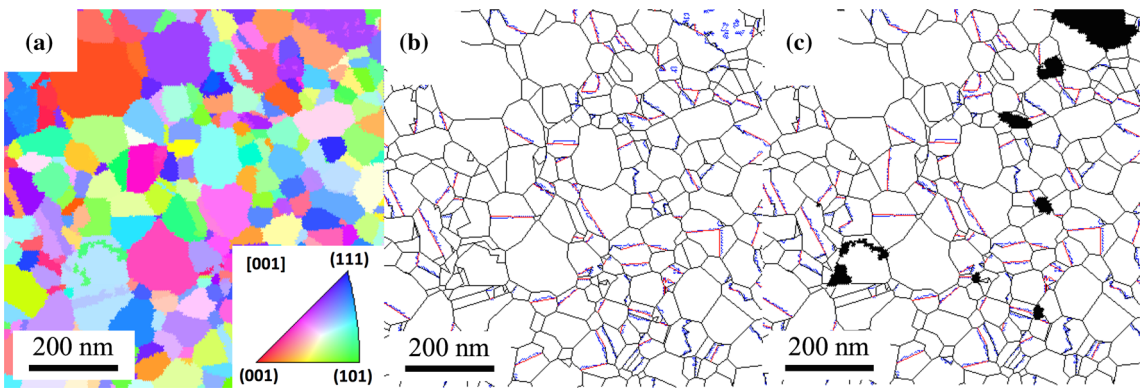

Figure 1 A representative orientation map of the as-deposited Al thin film. **a** Cleaned data with grains *colored* by the orientation in the normal direction according to the inset key. **b** Reconstructed boundary network in which *blue lines* represent Σ3 boundaries, *red lines* represent coherent twin boundaries (coherent Σ3 boundaries) and *black lines* represent all other grain boundary types. **c** Reconstructed boundary network after points with confidence index values smaller than 0.05 is removed (*colored black*).

three of these grain size values are given in Table 1 for the films in the current study, along with values from ref. 31 for comparison. In addition to the linear measures of grain size, grain size distributions were obtained. The reduced grain areas were determined as $\frac{A}{\langle A \rangle}$ and then used to determine the probability density of reduced area, using a bin size of 0.1. Since in a probability density plot, the total area under the distribution is equal to one, the probability density value at each given bin takes into account the choice of bin size. The choice of 0.1 for the bin size was made to allow comparison with probability densities for Al films reported previously by Barmak et al. [31]. The probability densities for the reduced diameters, $\frac{D}{\langle D \rangle}$, were fitted to the lognormal distribution in a manner similar to Ref. [31].

For the determination of GBCD, while TSL OIM™ has a built-in feature which can remove all grain boundaries related by a certain user-defined misorientation relationship, it will remove both real and pseudo-symmetry boundaries, biasing the GBCD results. In this work, the pseudo-symmetry boundaries are removed via a recently reported approach [34]. Regions affected by the pseudo-symmetry boundaries usually have very small confidence index values. Therefore, by removing orientation data points with a confidence index value smaller than 0.05, most pseudo-symmetry boundaries are successfully removed, as shown in Fig. 1c.

The GBCD from the Al thin films is compared to data from a bulk Al polycrystal of commercially pure alloy 1050. This alloy is typically more than 99.5% Al; Fe and Si are the principal impurities. The material was prepared by recrystallization and annealing at 400 °C and had an average grain size of approximately 23 μm obtained using the TSL software, and its GBCD has been reported previously; details of the preparation and features of the GBCD have already been published [15, 35]; these data are publicly available in the grain boundary data archive [36].

The GBCD, λ (Δg, n), is defined as the distribution of relative areas of different grain boundary types distinguished by lattice misorientation, specified by the three Euler angles, and grain boundary plane orientation, specified by the two spherical angles for the direction normal to the boundary plane. The five parameter GBCD can be measured either from the stereological interpretation of EBSD data from a plane [37] or by combining EBSD with serial sectioning [7, 8, 10]. However, the GBCD of a nanocrystalline material cannot be studied by EBSD because of the limited resolution of SEM-based EBSD [38, 39]. Here, we use TEM-based orientation mapping.

The GBCD of the nanocrystalline film is determined using an established stereological interpretation of the orientation data [37]. From a crystal orientation map, four out of the five parameters used to specify a grain boundary structure are provided. The unknown parameter is the inclination angle between the surface plane and the grain boundary plane; using enough data, the distribution of inclinations can be estimated stereologically. The process assumes that the bicrystals have a random orientation

Table 1 Al film thicknesses, h, annealing temperature, T, ratio of annealing temperature to melting point, T/T_m, annealing time, t, grain size calculated as the median of equivalent circle diameters, D_{med}, as mean of equivalent circle diameters, $\langle D \rangle$, and as equivalent circle diameter of mean grain area, $d_{\langle A \rangle}$, ratio of $d_{\langle A \rangle}$ to film thickness, median-to-mean ratio, $D_{med}/\langle D \rangle$ and the number of grains measured for each sample

h (nm)	T (°C)	T/T_m (K/K)	t (min)	D_{med} (nm)	$\langle D \rangle$ (nm)	$d_{\langle A \rangle}$ (nm)	$d_{\langle A \rangle}/h$ (nm/nm)	$D_{med}/\langle D \rangle$ (nm/nm)	No. grains	Ref.
25	400	0.72	120	36	40	43	1.7	0.91	2410	31
30	450	0.77	30	116	133	149	5	0.88	8185	
100	–	–	–	75	79	85	0.9	0.95	1931	
	400	0.72	30	87	95	104	1.0	0.92	1324	
			60	128	145	162	1.6	0.88	1113	
			120	134	145	159	1.6	0.92	1283	
			240	139	155	173	1.7	0.89	1516	
			600	143	159	179	1.8	0.90	759	
100	–	–	–	82	93	109	1.1	0.88	13839	This study
	400	0.72	30	116	131	152	1.5	0.89	13581	
			150	121	136	157	1.6	0.89	9356	

distribution. It has been shown by Saylor et al. [37] that mild orientation texture does not have a significant effect on the result. While the degree of texture that significantly affects the result has not been clearly established, simulations involving data from a cubic material that had a preferred orientation with an intensity of 2.4 multiples of random distribution (MRD) showed that this did not significantly affect the result.

Typical orientation maps of the as-deposited and annealed Al thin film samples are illustrated in Fig. 2a–c. The as-deposited thin film Al sample had inhomogeneous texture, ranging from random to a preference for having ⟨111⟩ parallel to the sample normal (fiber texture). When the data from nine fields of view each containing more than 1500 grains with a total sampled area of approximately 129 μm^2 are combined, the ⟨111⟩ orientation has a preferred orientation of 2.3 MRD (see Fig. 2d). This indicates only a modest degree of texture when compared to the strong ⟨111⟩ fiber texture typically found in annealed, vacuum-deposited Al films [31]. The annealed films, on the other hand, had ⟨111⟩ preferred orientations of 5.4 MRD (30-min annealed) and 6.0 MRD (150-min annealed). Because of the strength of the texture in the annealed films, a stereological estimate of the grain boundary plane distribution would be biased. However, the texture in the as-deposited film is low enough to accurately compute the grain boundary plane distribution [37], which will be compared to that of the bulk sample. The GBCD of the Al film was computed from 79,000 grain boundary line segments, and the GBCD of the bulk aluminum was computed from 77,000 grain boundary line segments. A similar number of segments were used to compute the disorientation angle distributions (Fig. 6) and the misorientation axis–angle distributions (Fig. 7) for the annealed samples.

Results

A section of the orientation map in Fig. 2a is magnified to show more details in Fig. 3a. The diffraction patterns from the grains labeled 1, 2 and 3 are shown in Fig. 3b–d, respectively. There is no evidence of overlapping diffraction patterns, indicating that the grains are continuous through the film thickness.

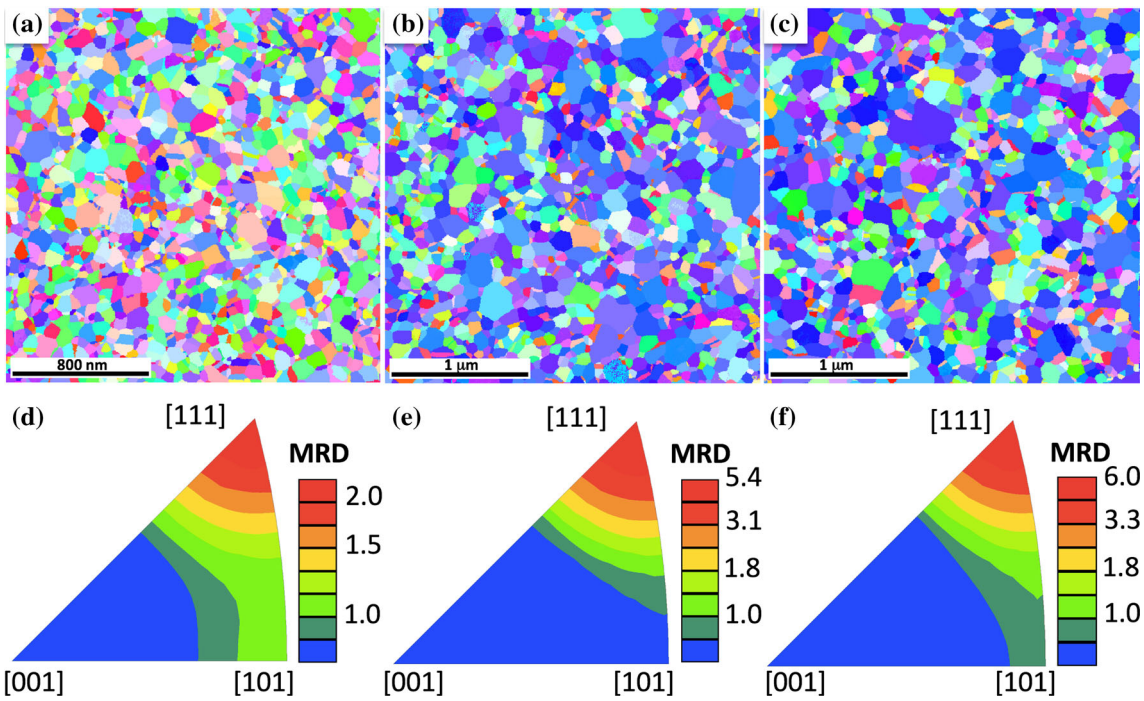

Figure 2 **a**–**c** Typical orientation maps of the 100-nm Al thin films. **a** As-deposited, **b** annealed at 400 °C for 30 min and **c** annealed at 400 °C for 150 min. **d**–**f** Inverse pole figures for the Al film along the normal direction. **d** As-deposited (based on nine maps similar to the one shown in (**a**)), **e** annealed at 400 °C for 30 min (based on eleven maps similar to the one shown in (**b**)), **f** annealed at 400 °C for 150 min (based on eight maps similar to the one shown in (**c**)).

Note that many of the grains are cut by long straight boundaries; these are twin boundaries, as illustrated in Fig. 1b.

Table 1 lists the grain sizes of the films as a function of annealing time obtained from the orientation maps, along with other microstructural metrics and the numbers of grains measured for each film. Data for the Al films reported previously by Barmak et al. [31] are also given in Table 1 for comparison. The equivalent circle diameter of the mean area as a function of annealing time at 400 °C is plotted in Fig. 4. The figure shows the grain size in the as-deposited and 30-min annealed samples to be larger when compared to the study of Barmak et al. [31]. However, at 150 min, the grain size is comparable to that for 120-min annealed sample of Ref. [31]. Note that the grain size in the film annealed for 150 min (157 nm) is only 3% larger than the grain size of the sample annealed for 30 min (152 nm).

The prior study of Barmak et al. [31] showed evidence of the stagnation of grain growth as seen in Fig. 4, and thus, based on the trend in grain size as a function of annealing time, it is reasonable to conclude that the samples in the current study have also reached the stagnant stage and have done so after only 30 min of annealing. This conclusion is further supported by the close agreement of the probability densities for reduced grain areas between the 30- and 150-min annealed samples of the current study and those for the Al films reported by Barmak et al. [31] in Fig. 5. In addition, the grain size distributions, with the measure of grain size as reduced equivalent circle diameters, $D/\langle D\rangle$, for the current study were found to be lognormal and in good agreement with the universal distribution reported by Barmak et al. [31] (Plots not shown). For the universal distribution, the median-to-mean grain size ratio, $D_{\mathrm{med}}/\langle D\rangle$, was found to be 0.89, with the individual data sets having ratios of 0.87 ± 0.3 [40]. As can be seen in Table 1, this ratio for the samples in the current study is 0.88 or 0.89, in good agreement with the prior studies summarized in [31].

The distribution of grain boundary disorientation angles (minimum misorientation angles) for the thin film and bulk samples is compared in Fig. 6. The annealed samples have distributions that are nearly identical. The as-deposited sample is also similar, but the fraction of boundaries with 39° and 60° disorientations are greater in the as-deposited film. The bulk sample differs from the thin films in two significant ways. First, the peak at the 60° disorientation is more than seven times larger in the film than in the bulk sample. As we shall see, this peak is associated with twin boundaries. The second difference is that

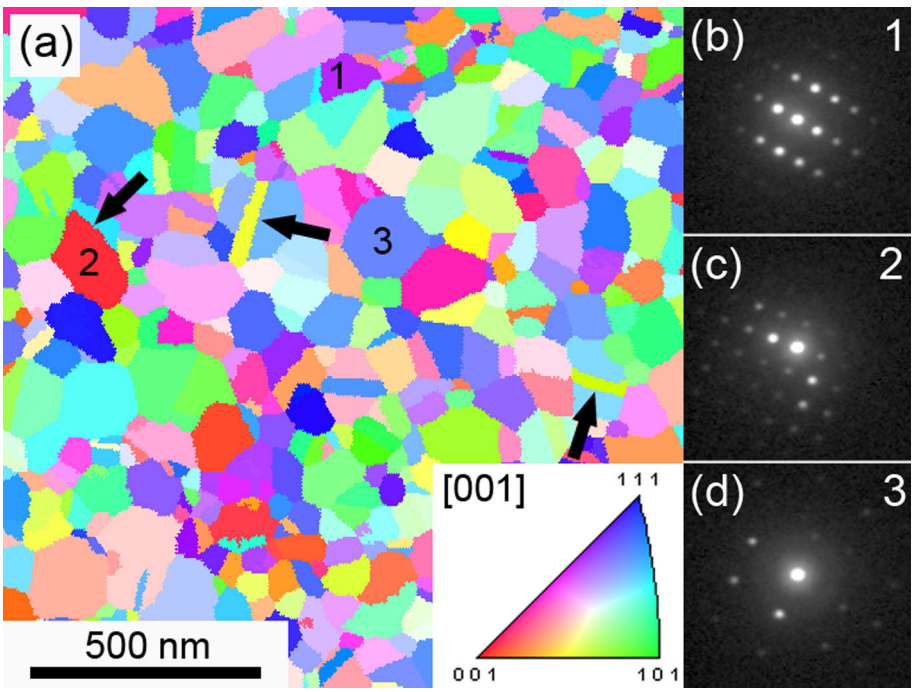

Figure 3 **a** Orientation map of the as-deposited Al film. Diffraction patterns in (**b**)–(**d**) correspond to the grains labeled *1*, *2* and *3*. The *black arrows* denote examples of long twin boundaries that cut through grains.

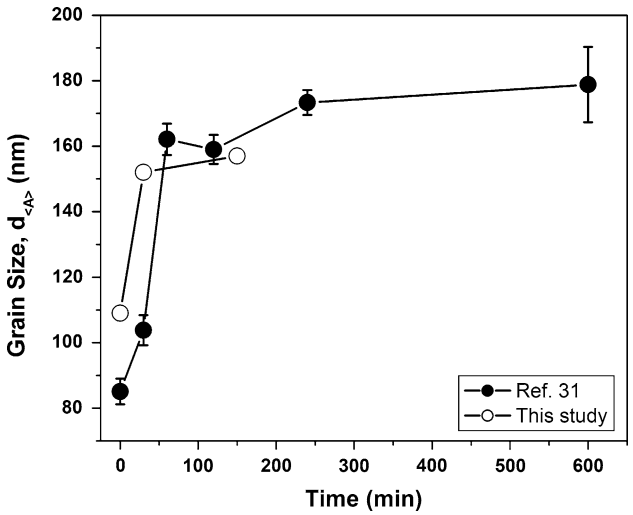

Figure 4 Grain size as equivalent circle diameter of mean area, $d_{\langle A \rangle}$, is plotted as a function of annealing time at 400 °C for the 100-nm-thick Al films in the current study. The data for an Al film nominally 100 nm in thickness and annealed at 400 °C from Ref. [31] are given for comparison. The *error bars* are the 2σ values at a 95% confidence level for the given grain population [30]. For the data set in the current work, the error bars are smaller than the size of the data points. The *lines* are drawn to guide the eye.

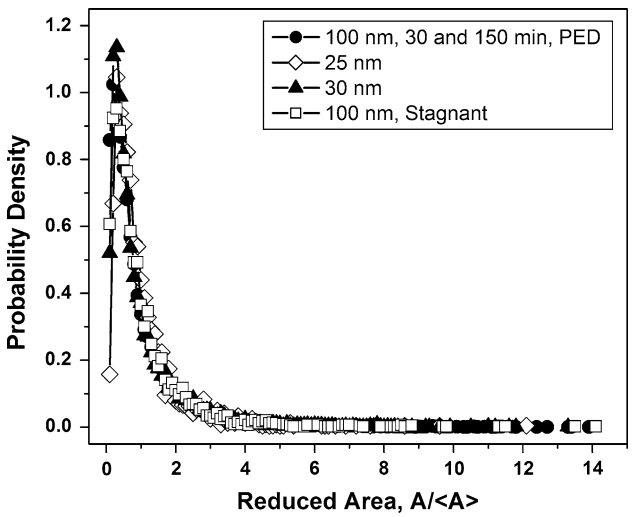

Figure 5 Probability density of reduced grain area for the 30- and 150-min annealed Al films of the current study is compared with the densities for the Al films in the prior report of Barmak et al. [31]. A bin size of 0.1 was used for this plot. In this plot, A is the area of a given grain, and $\langle A \rangle$ is the mean area. The reduced area, $A/\langle A \rangle$, is a dimensionless parameter. The data for the current study were obtained using a precession electron diffraction (PED) crystal orientation mapping-based method, whereas prior studies reported in [31] used image-based methods.

the bulk sample has an enhanced population of low-angle boundaries, compared to the thin film samples, in the range between 5° and 15°.

Sections of the grain boundary axis–angle distributions for the as-deposited film and the bulk sample are shown in Fig. 7. The sections for the annealed samples were the same as the as-deposited sample, but with small differences in the amplitudes of the maxima. For disorientations of 10°, the maximum is at [111] for both the film and bulk samples. The values of the distribution for this disorientation for all axes are greater for the bulk sample, consistent with the disorientation angle distribution (Fig. 6), which shows a local maximum at 10° for the bulk sample. At 39°, the maximum is again at [111] for the both film and bulk. However, for the film, there is also a local maximum at [101], which is the Σ9 grain boundary misorientation. This is consistent with the local maximum at 39° for the film in the disorientation angle distribution (Fig. 6). At the 50° misorientation, there is a significant difference between the film and the bulk; the distribution for the film maximizes at [101] with a value of 3.2 MRD (this is the Σ11 misorientation), and in the bulk it maximizes at [111] with a value of 2.2 MRD. The greater maximum for the film is consistent with the disorientation angle distribution in Fig. 6. In the section at 60° for the thin film (bulk), the maximum is at the [111] orientation with a value of 60 (3.6) MRD. Therefore, the majority of all grain boundaries with a 60° misorientation are Σ3 grain boundaries.

The grain boundary plane distribution, independent of misorientation, is illustrated in Fig. 8. For both the thin film and the bulk sample, the distributions are similar with maxima at the (111) orientation. Considering that the most common misorientation axis is [111] and the most common grain boundary plane is (111), then boundaries with (111) twist character are the most common. This is a common finding for metals with the FCC structure [29, 41]. Note that the maximum in the grain boundary plane distribution is higher for the thin film sample. This is likely the result of the higher concentration of coherent twins in the thin film sample, which is quantified below.

The distributions of grain boundary planes at fixed misorientations about the [111] axis (Σ1, Σ13a, Σ7 and Σ3) are shown in Fig. 9. The maximum for each distribution is at the (111) position; because the grain boundary planes are perpendicular to the [111] misorientation axes, these are all twist boundaries.

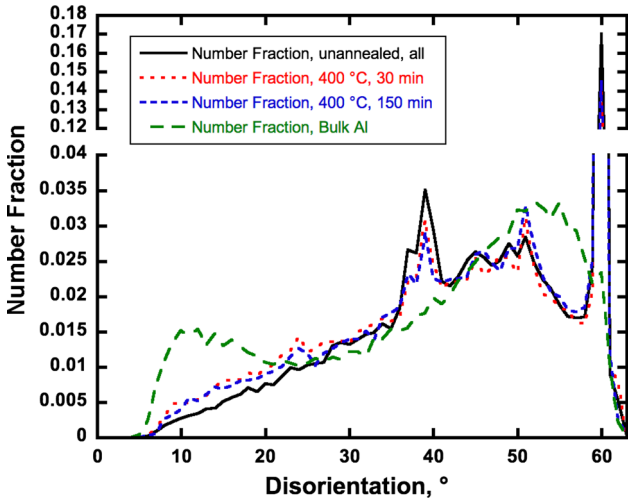

Figure 6 Disorientation angle distributions for the different samples. The disorientation values are classified discretely in bins with a 1° width. As-deposited thin film (unannealed): *solid black line*. Thin film annealed for 30 min at 400 °C: *red dashed line* with the shortest dashes. Thin film annealed for 150 min at 400 °C: *blue dashed line* with intermediate length dashes. Bulk aluminum: *green dashed line* with the *longest dashes*.

These results are consistent with Fig. 8, which shows that (111) is the most common grain boundary plane orientation when all misorientations are considered. For the case of the Σ3 boundary, this shows that they are mostly coherent twins. Note that the maximum at the coherent twin position for the thin film sample is 700 MRD, more than 20 times the maximum in the bulk sample (30 MRD). The distribution of grain boundary planes for the bulk sample at 5° about [111] has secondary maxima at {111} positions that are not observed in the thin film sample. With the exception of the aforementioned secondary maxima and the large intensity difference at the coherent twin position, the distributions in the bulk and thin film are similar.

Two examples of the grain boundary plane distribution at other misorientations are shown in Fig. 10. The Σ19a misorientation is an example of a boundary that occurs infrequently; the maxima in the distribution for the as-deposited film do not exceed 2.2 MRD. Although not exactly the same, the grain

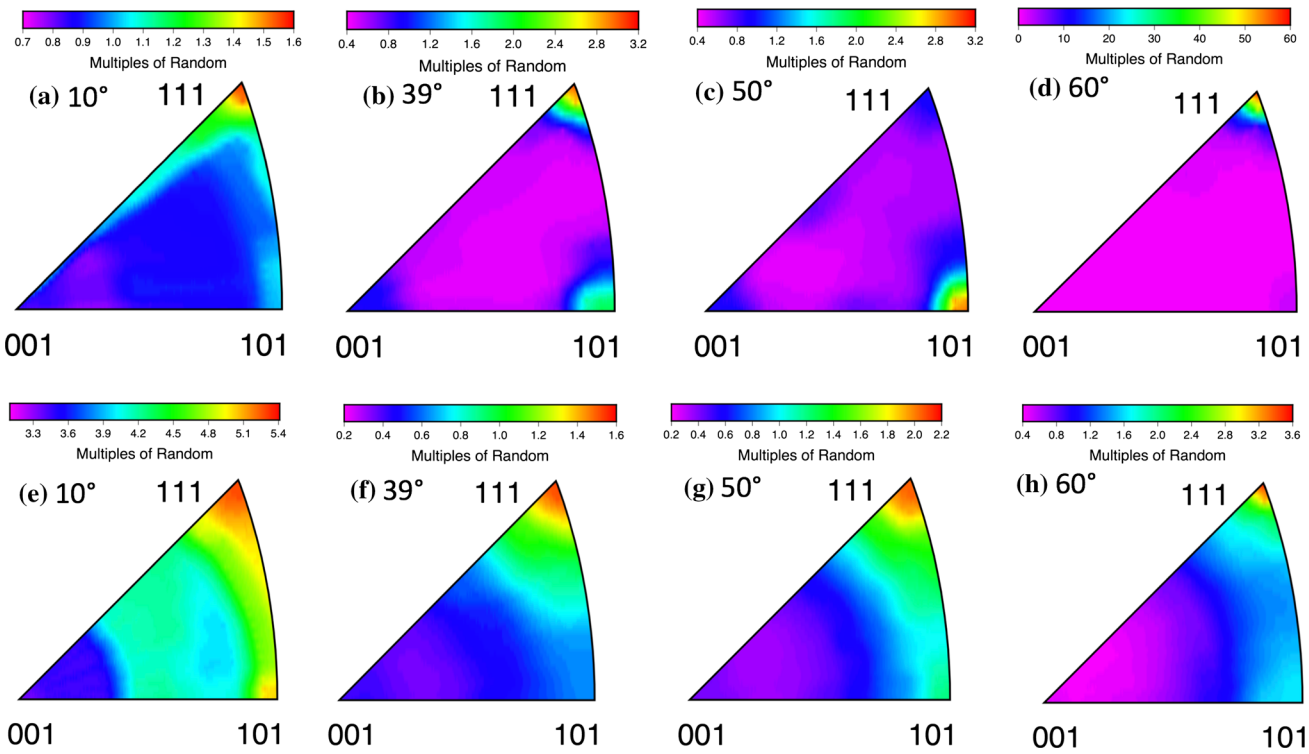

Figure 7 Distributions of grain boundaries in axis–angle space for the as-deposited thin film (**a**–**d**) and bulk (**e**–**h**) samples. In each section, all possible axes are shown and the population is plotted at 10° (**a**, **e**), 39° (**b**, **f**), 50° (**c**, **g**) and 60° (**d**, **h**). The distributions are discrete and calculated with a resolution of 7.5°.

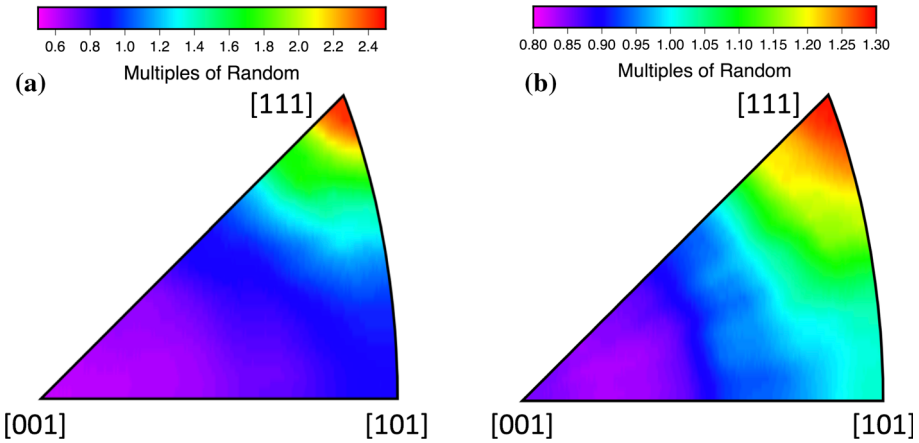

Figure 8 Distribution of grain boundary planes independent of misorientation for the as-deposited thin film (**a**) and bulk (**b**) samples. The distribution is discrete and was calculated with a resolution of 7.5°.

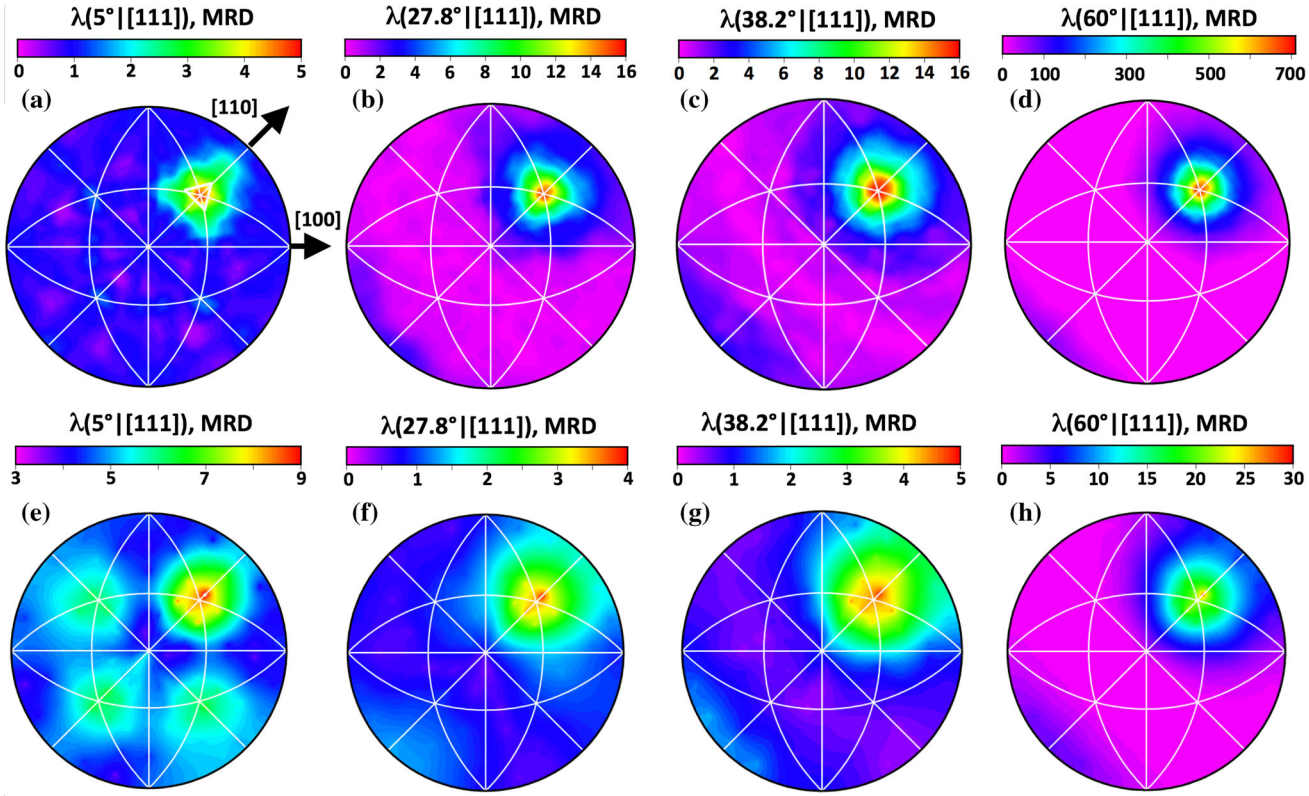

Figure 9 Distribution of grain boundary planes at fixed misorientations for the as-deposited thin film (**a**–**d**) and bulk (**e**–**h**) samples. The misorientations are Σ1 (**a**, **e**), Σ13a (**b**, **f**), Σ7 (**c**, **g**) and Σ3 (**d**, **h**). The [110] and [100] directions are in the plane and marked with *black arrows* in (**a**). The [111] direction is marked by a *white triangle*. The same convention is used in all of the grain boundary plane distributions.

boundary plane distributions for the Σ19a misorientation are similar. For the thin film, the maxima occur for planes that are perpendicular to the misorientation axis, in the [110] zone. There are weaker local maxima at several other orientations, including (111) and $(\bar{1}\bar{1}0)$. For the bulk sample, on the other hand, the maxima are at these positions [(111) and $(\bar{1}\bar{1}1)$] and there are weaker local maxima along the [110] zone. These differences, of no more than 1 MRD, are not thought to be significant. The distributions of grain boundary planes are also similar for the Σ11 grain boundary, where the maximum in the distributions of the bulk and film samples are at the position of the $(1\bar{1}3)$ symmetric tilt boundary.

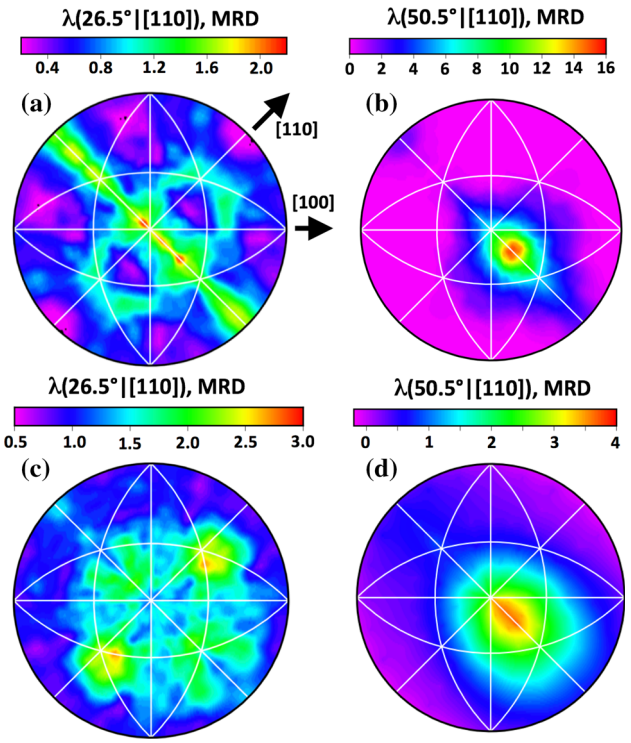

Figure 10 Distribution of grain boundary planes at fixed misorientations for the as-deposited thin film (**a**, **b**) and bulk (**c**, **d**) samples. The misorientations are Σ19a (**a**, **c**) and Σ11a (**b**, **d**). The [110] and [100] directions are in the plane and marked with *black arrows* in (**a**).

To make a more quantitative comparison between the distributions, we average the populations of all grain boundaries that have a population that is within an interval of 0.25 MRD in the Al thin film. We then average the populations of the boundaries with the same crystallographic parameters in the bulk Al. When this is repeated for all possible intervals and these two averages are plotted on a graph, the result is shown in Fig. 11a. The strong linear characteristic of the graph illustrates that if a boundary is highly populated in the nanocrystalline sample, it is also highly populated in the microcrystalline sample. However, Fig. 11a is biased to show the population of Σ3 boundaries, which in the film are all boundaries with populations greater than 30 MRD. In this domain, the slope is much less than unity. However, if one examines the correlations among the non-Σ3 boundaries (see Fig. 9b), the data are correlated with a slope more nearly equal to one. The positive deviation from the ideal correlation in Fig. 11b is the result of the difference in the concentration of Σ3 boundaries in the two samples; the relative areas of the non-Σ3 boundaries are higher in the bulk sample, because a smaller fraction of the total area is made up of Σ3 boundaries. The comparison in Fig. 11 shows that the similarity of the distributions illustrated in Figs. 9 and 10 is representative of the entire data set. Specifically, the grain boundary character distributions in thin film nanocrystalline Al and bulk microcrystalline Al are similar, except that there are many more twins in the thin film.

Discussion

With the exception of the high concentration of twins in the thin film samples, the populations of grain boundaries in the nanocrystalline sample and the microcrystalline sample are similar. The GBCD is dominated by misorientations about the [111] axis and of these boundaries, twist boundaries are the most common. It has been shown that the populations of grain boundaries in Al are inversely correlated to the calculated grain boundary energies [35]. The present work indicates that this distribution can be achieved at the very earliest stages of grain growth, when the average grain size is approximately 100 nm. The distribution is thought to develop by the elimination of relatively higher energy grain boundaries in favor of relatively lower energy grain boundaries [42]. A simulation of this process indicated that the size invariant distribution develops during a doubling of the grain size by normal grain growth [43]. It has also been observed in simulations and experiments that, after extensive grain growth, the fraction of low disorientation angle grain boundaries (which have relatively low energies) exceeds that expected in a random distribution [44]. This is a plausible reason for the elevated population of low-angle grain boundaries in the bulk sample.

The high concentration of twins in the nanocrystalline Al sample must be noted as both unusual and surprising. While twins are common in other FCC metals with lower stacking fault energies, their populations are not as large in Al. The stacking fault energy in Al has been calculated to be 66–280 mJ/m^2 [45–48]. For comparison, the stacking fault energy of Cu and Ag, which has highly twinned microstructures, calculated via different approaches is 14–78 and 1–22 mJ/m^2, respectively [49–51]. While Al can twin by deformation [52–54], these films were heated to 400 °C, well above the temperature at which

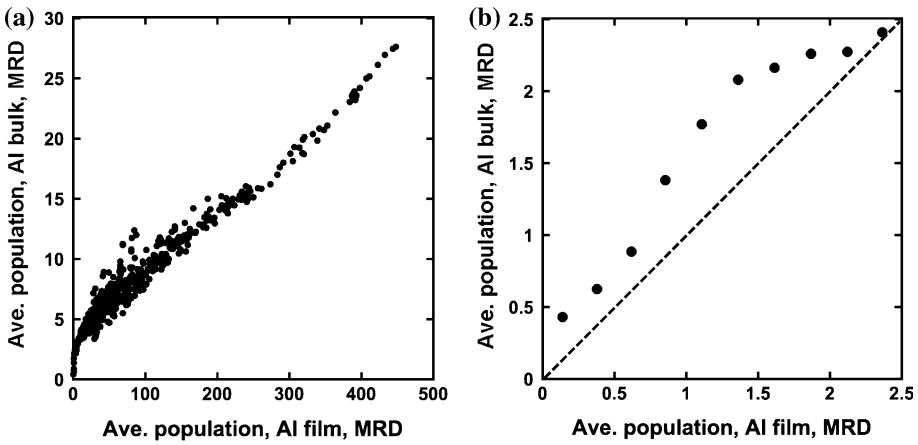

Figure 11 **a**–**b** Correlation of the populations of the same boundaries in the as-deposited film and bulk Al. The average of all grain boundaries in the thin film with populations in an interval of 0.25 MRD is found, and the populations of the same boundaries in bulk Al are averaged. Each point on the plot represents the two averages in a single population interval. In (**b**), the *dashed line* has a slope of one and represents the ideal correlation and is added as a guide to the eye.

stresses in Al are relaxed [55]. This, and the fact that twins are seen in the as-deposited (unannealed) film, suggests that the twins were not mechanically introduced during annealing.

Other materials that have significant numbers of Σ3 boundaries are Si [13] and Cu [30]. In these cases, it has been noted the high concentration of Σ3 boundaries leads to an elevated concentration of Σ9 boundaries. When two Σ3 grain boundaries meet, a Σ9 boundary is formed [56]. If distributed randomly, one would expect the number fraction of Σ3 grain boundaries squared (the probability that they intersect) would equal the concentration of Σ9 boundaries. This is approximately correct for Si [13] and Cu [30]. Here, however, there are fewer Σ9 grain boundaries than would be expected based on this line of reasoning. In the as-deposited sample, 20% of all boundaries are Σ3 type, suggesting that 4% of the boundaries should be Σ9. In fact, only 2.7% are Σ9. In the sample annealed for 30 (150) minutes, the Σ3 concentration is 17 (18) % and the Σ9 concentration is 1.9 (1.7) %. The lower concentration of Σ9 boundaries suggests that the Σ3 boundaries are not randomly distributed, and this might be connected to their mechanism of formation during the growth process.

There are interesting changes in the microstructure during annealing. In the first 30 min of annealing, the average grain diameter increases from 109 to 152 nm, implying that (assuming a columnar, 2D grain structure) half of the grains and grain boundaries are eliminated by grain growth. The ⟨111⟩ grain orientation texture also strengthens considerably, from about 2 MRD to about 6 MRD.

Grain growth in thin films can be affected by driving forces other than grain boundary energy reduction. Two of the most important of these driving forces are surface and elastic–strain energies. [57] The reduction in these energies results in the growth of a subpopulation of grains and leads to the development of film texture. The calculated texture map for Al films [40] shows that for the film thickness, and deposition and annealing temperature used in the current study, surface energy reduction dominates and thus the ⟨111⟩ fiber texture of the film is strengthened as grain growth proceeds.

At the same time, the concentration of Σ3 boundaries decreases. The length fraction of Σ3 boundaries decreases from 24.5% in the as-deposited sample to 18.8% (21.1%) in the sample annealed for 30 (150) minutes at 400 °C. Because the Σ3 boundaries are among the lowest energy boundaries, it is unusual that their concentration decreases during growth. However, this might be related to the sample geometry and the elimination of excess grain boundary energy during grain growth. Note that the grain boundary area (and energy) is minimized when the boundaries are perpendicular to the free surface of the sample. However, because the preferred grain orientation is ⟨111⟩, a twin grain boundary is geometrically constrained to be inclined with respect the surface normal, having an area that is 15% greater than a boundary that is perpendicular surface. The

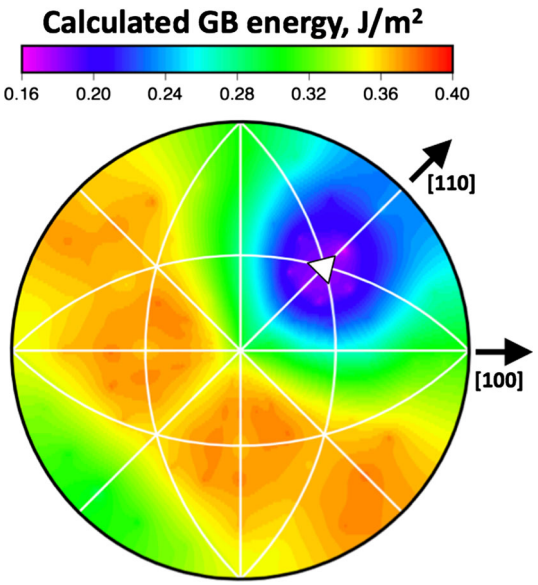

Figure 12 Energies of the Σ3 grain boundaries in Al calculated by Olmsted et al. [58]. The misorientation axis is marked by a *triangle*. The energies reach a maximum along the [111] zone, which are the positions of the [111] tilt boundaries.

range of energies of Σ3 grain boundaries is illustrated in Fig. 12. This is similar to the range of energy of other types of grain boundaries in Al [58]. Therefore, it is possible that a boundary that is normal to the sample surface, with a higher energy per unit area, could be favored over a grain boundary with a lower energy per unit area, but that is constrained to be inclined and thus have a higher total energy in the film. Therefore, the combination of film texture and geometry might disfavor low-energy boundaries that are constrained to be inclined with respect to the sample surface. The grain boundary energy distribution in Fig. 12 also indicates that tilt grain boundaries between two [111] oriented grains (those favored by the geometry of the [111] textured film) have a relatively high energy, at least for Σ3 boundaries. In Fig. 12, the tilt boundaries are those perpendicular to the [111] direction.

The question arises as to how such a high concentration of Σ3 grain boundaries forms in the Al film, while boundaries of the same crystallography occur much less frequently in bulk Al. This is currently not known but might be related to the evolution of film structure during deposition [57]. Al films, vapor deposited on amorphous substrates such as oxidized silicon wafers, as in the current study, form by nucleation, growth and coalescence of metal islands. When an island pair comes into touching contact, the free surfaces snap together and form a grain boundary in place of the two free surfaces [59]. The grain boundary energy is much less than the energy of the two free surfaces, with {111} boundary planes for both grains providing the lowest boundary energy among all possible boundaries. The {111} boundary continues to lengthen as the film thickens, but once the film is fully coalesced, the reduction in surface, strain and grain boundary energies will drive grain growth and reduce the overall {111} boundary area, as noted earlier. If this is the mechanism for formation of twin boundaries in thin films, then it is unclear whether it is possible to replicate such a high Σ3 concentration in a bulk material.

Conclusions

The grain boundary populations in nanocrystalline Al and microcrystalline Al are correlated. The populations are quite similar, except for the unusually high population of twins in the thin film sample (24.5% by length). Assuming the grain boundary character distribution is determined by the energy anisotropy, and these findings indicate the steady-state distribution (for all but the Σ3 misorientation) can be reached at grain sizes as small as approximately 100 nm. When the grains grow after deposition, the reduction in surface and interface energy drives the growth of ⟨111⟩ grain orientations and strengthening of the ⟨111⟩ fiber texture. The geometric constraints imposed by the texture and form factor of the film likely contribute to a reduction in the fraction of Σ3 misorientations during post-deposition grain growth.

Acknowledgements

Financial support of the SRC, Task 1292.008, 2121.001, 2323.001 and of the MRSEC programs of the NSF under DMR-0520425 and DMR-1420634 is gratefully acknowledged. G.S.R. acknowledges support from the National Science Foundation under Grant DMR 1628994 and use of the Materials Characterization Facility at Carnegie Mellon University supported by Grant MCF-677785.

Compliance with ethical standards

Conflicts of interest No conflicts of interest exist for any of the authors.

References

[1] Kim CS, Rollett AD, Rohrer GS (2006) Grain boundary planes: new dimensions in the grain boundary character distribution. Scripta Mater 54:1005–1009. doi:10.1016/j.scriptamat.2005.11.071

[2] Lee SB, Key TS, Liang Z et al (2013) Microstructure design of lead-free piezoelectric ceramics. J Eur Ceram Soc 33:313–326. doi:10.1016/j.jeurceramsoc.2012.08.015

[3] Lu L, Shen YF, Chen XH, Qian LH, Lu K (2004) Ultrahigh strength and high electrical conductivity in copper. Science 304:422–426. doi:10.1126/science.1092905

[4] Randle V (2004) Twinning-related grain boundary engineering. Acta Mater 52:4067–4081. doi:10.1016/j.actamat.2004.05.031

[5] Sun T, Yao B, Warren AP et al (2010) Surface and grain-boundary scattering in nanometric cu films. Phys Rev B. doi:10.1103/PhysRevB.81.155454

[6] Adams BL, Wright SI, Kunze K (1993) Orientation imaging—the emergence of a new microscopy. Metall Trans a-Phys Metall Mater Sci 24:819–831

[7] Beladi H, Rohrer GS (2013) The relative grain boundary area and energy distributions in a ferritic steel determined from three-dimensional electron backscatter diffraction maps. Acta Mater 61:1404–1412. doi:10.1016/j.actamat.2012.11.017

[8] Dillon SJ, Rohrer GS (2009) Characterization of the grain-boundary character and energy distributions of yttria using automated serial sectioning and ebsd in the fib. J Am Ceram Soc 92:1580–1585. doi:10.1111/j.1551-2916.2009.03064.x

[9] Rohrer GS, Li J, Lee S, Rollett AD, Groeber M, Uchic MD (2010) Deriving grain boundary character distributions and relative grain boundary energies from three-dimensional ebsd data. Mater Sci Technol 26:661–669. doi:10.1179/026708309X12468927349370

[10] Saylor DM, Morawiec A, Rohrer GS (2002) Distribution and energies of grain boundaries in magnesia as a function of five degrees of freedom. J Am Ceram Soc 85:3081–3083

[11] Rohrer GS, Saylor DM, El Dasher B, Adams BL, Rollett AD, Wynblatt P (2004) The distribution of internal interfaces in polycrystals. Zeitschrift Fur Metallkunde 95:197–214

[12] Beladi H, Rohrer GS (2013) The distribution of grain boundary planes in interstitial free steel. Metall Mater Trans A Phys Metall Mater Sci 44A:115–124. doi:10.1007/s11661-012-1393-0

[13] Ratanaphan S, Yoon Y, Rohrer GS (2014) The five parameter grain boundary character distribution of polycrystalline silicon. J Mater Sci 49:4938–4945. doi:10.1007/s10853-014-8195-2

[14] Saylor DM, El Dasher B, Sano T, Rohrer GS (2004) Distribution of grain boundaries in srtio3 as a function of five macroscopic parameters. J Am Ceram Soc 87:670–676

[15] Saylor DM, El Dasher BS, Rollett AD, Rohrer GS (2004) Distribution of grain boundaries in aluminum as a function of five macroscopic parameters. Acta Mater 52:3649–3655. doi:10.1016/j.actamat.2004.04.018

[16] Rohrer GS (2011) Grain boundary energy anisotropy: a review. J Mater Sci 46:5881–5895. doi:10.1007/s10853-011-5677-3

[17] Rohrer GS (2011) Measuring and interpreting the structure of grain-boundary networks. J Am Ceram Soc 94:633–646. doi:10.1111/j.1551-2916.2011.04384.x

[18] Rauch EF, Barmak K, Ganesh K et al (2011) Tem automated orientation and phase mapping for thin film applications. Microsc Microanal 17:1086–1087

[19] Rauch EF, Dupuy L (2005) Rapid spot diffraction patterns identification through template matching. Arch Metall Mater 50:87–99

[20] Rauch EF, Portillo J, Nicolopoulos S, Bultreys D, Rouvimov S, Moeck P (2010) Automated nanocrystal orientation and phase mapping in the transmission electron microscope on the basis of precession electron diffraction. Zeitschrift Fur Kristallographie 225:103–109. doi:10.1524/zkri.2010.1205

[21] Rauch EF, Veron M (2005) Coupled microstructural observations and local texture measurements with an automated crystallographic orientation mapping tool attached to a tem. Materialwiss Werkstofftech 36:552–556. doi:10.1002/mawe.200500923

[22] Carpenter JS, Liu X, Darbal A et al (2012) A comparison of texture results obtained using precession electron diffraction and neutron diffraction methods at diminishing length scales in ordered bimetallic nanolamellar composites. Scripta Mater 67:336–339. doi:10.1016/j.scriptamat.2012.05.018

[23] Darbal A, Ganesh K, Barmak K et al (2011) Grain boundary characterization of nanocrystalline cu from the stereological analysis of transmission electron microscope orientation maps. Microsc Microanal 17:1416–1417

[24] Darbal AD, Ganesh KJ, Liu X et al (2013) Grain boundary character distribution of nanocrystalline cu thin films using stereological analysis of transmission electron microscope orientation maps. Microsc Microanal 19:111–119. doi:10.1017/s1431927612014055

[25] Liu X, Choi D, Beladi H, Nuhfer NT, Rohrer GS, Barmak K (2013) The five-parameter grain boundary character distribution of nanocrystalline tungsten. Scripta Mater 69:413–416. doi:10.1016/j.scriptamat.2013.05.046

[26] Liu X, Nuhfer NT, Rollett AD et al (2014) Interfacial orientation and misorientation relationships in nanolamellar Cu/Nb composites using transmission-electron-microscope-based orientation and phase mapping. Acta Mater 64:333–344. doi:10.1016/j.actamat.2013.10.046

[27] Liu X, Nuhfer NT, Warren AP, Coffey KR, Rohrer GS, Barmak K (2015) Grain size dependence of the twin length fraction in nanocrystalline cu thin films via transmission electron microscopy based orientation mapping. J Mater Res 30:528–537. doi:10.1557/jmr.2014.393

[28] Liu X, Warren AP, Nuhfer NT, Rollett AD, Coffey KR, Barmak K (2014) Comparison of crystal orientation mapping-based and image-based measurement of grain size and grain size distribution in a thin aluminum film. Acta Mater 79:138–145. doi:10.1016/j.actamat.2014.07.014

[29] Randle V, Rohrer GS, Miller HM, Coleman M, Owen GT (2008) Five-parameter grain boundary distribution of commercially grain boundary engineered nickel and copper. Acta Mater 56:2363–2373. doi:10.1016/j.actamat.2008.01.039

[30] Ratanaphan S, Raabe D, Sarochawikasit R, Olmsted DL, Rohrer GS, Tu KN (2017) Grain boundary character distribution in electroplated nanotwinned copper. J Mater Sci 52:4070–4085. doi:10.1007/s10853-016-0670-5

[31] Barmak K, Eggeling E, Kinderlehrer D et al (2013) Grain growth and the puzzle of its stagnation in thin films: the curious tale of a tail and an ear. Prog Mater Sci 58:987–1055. doi:10.1016/j.pmatsci.2013.03.004

[32] Yao B, Petrova RV, Vanfleet RR, Coffey KR (2006) A modified back-etch method for preparation of plan-view high-resolution transmission electron microscopy samples. J Electron Microsc 55:209–214. doi:10.1093/jmicro/dfl027

[33] Wright SI, Larsen RJ (2002) Extracting twins from orientation imaging microscopy scan data. J Microsc Oxford 205:245–252. doi:10.1046/j.1365-2818.2002.00992.x

[34] Bojarski SA, Stuer M, Zhao Z, Bowen P, Rohrer GS (2014) Influence of Y and La additions on grain growth and the grain-boundary character distribution of alumina. J Am Ceram Soc 97:622–630. doi:10.1111/jace.12669

[35] Holm EA, Rohrer GS, Foiles SM, Rollett AD, Miller HM, Olmsted DL (2011) Validating computed grain boundary energies in fcc metals using the grain boundary character distribution. Acta Mater 59:5250–5256. doi:10.1016/j.actamat.2011.05.001

[36] Rohrer GS (2015) http://mimp.materials.cmu.edu/~gr20/Grain_Boundary_Data_Archive/

[37] Saylor DM, El-Dasher BS, Adams BL, Rohrer GS (2004) Measuring the five-parameter grain-boundary distribution from observations of planar sections. Metall Mater Trans A Phys Metall Mater Sci 35A:1981–1989

[38] Dingley D (2004) Progressive steps in the development of electron backscatter diffraction and orientation imaging microscopy. J Microsc Oxford 213:214–224. doi:10.1111/j.0022-2720.2004.01321.x

[39] Humphreys FJ (2001) Review—grain and subgrain characterisation by electron backscatter diffraction. J Mater Sci 36:3833–3854. doi:10.1023/a:1017973432592

[40] Barmak K Coffey KR (eds) (2014) Metallic films for electronic, optical and magnetic applications Woodhead Publishing, Cambridge

[41] Beladi H, Nuhfer NT, Rohrer GS (2014) The five-parameter grain boundary character and energy distributions of a fully austenitic high-manganese steel using three dimensional data. Acta Mater 70:281–289. doi:10.1016/j.actamat.2014.02.038

[42] Dillon SJ, Rohrer GS (2009) Mechanism for the development of anisotropic grain boundary character distributions during normal grain growth. Acta Mater 57:1–7. doi:10.1016/j.actamat.2008.08.062

[43] Gruber J, George DC, Kuprat AP, Rohrer GS, Rollett AD (2005) Effect of anisotropic grain boundary properties on grain boundary plane distributions during grain growth. Scripta Mater 53:351–355. doi:10.1016/j.scriptamat.2005.04.004

[44] Gruber J, Miller HM, Hoffmann TD, Rohrer GS, Rollett AD (2009) Misorientation texture development during grain growth. Part I: simulation and experiment. Acta Mater 57:6102–6112. doi:10.1016/j.actamat.2009.08.036

[45] Denteneer PJH, Soler JM (1991) Defect energetics in aluminum. J Phys Condens Matter 3:8777–8792. doi:10.1088/0953-8984/3/45/003

[46] Hammer B, Jacobsen KW, Milman V, Payne MC (1992) Stacking-fault energies in aluminum. Journal of Physics-Condensed Matter 4:10453–10460. doi:10.1088/0953-8984/4/50/033

[47] Wright AF, Daw MS, Fong CY (1992) Theoretical investigation of (111)-stacking faults in aluminum. Philos Mag A Phys Condens Matter Struct Defects Mech Prop 66:387–404

[48] Xu JH, Lin W, Freeman AJ (1991) Twin-boundary and stacking-fault energies in Al and Pd. Phys Rev B 43:2018–2024. doi:10.1103/PhysRevB.43.2018

[49] Gallaghe PC (1970) Influence of alloying, temperature, and related effects on stacking fault energy. Metall Trans 1:2429–2430

[50] Meyers MA, Murr LE (1978) Model for formation of annealing twins in fcc metals and alloys. Acta Metall 26:951–962. doi:10.1016/0001-6160(78)90046-9

[51] Oh DJ, Johnson RA (1988) Simple embedded atom method model for fcc and hcp metals. J Mater Res 3:471–478. doi:10.1557/jmr.1988.0471

[52] Chen MW, Ma E, Hemker KJ, Sheng HW, Wang YM, Cheng XM (2003) Deformation twinning in nanocrystalline aluminum. Science 300:1275–1277. doi:10.1126/science.1083727

[53] Narayan J, Zhu YT (2008) Self-thickening, cross-slip deformation twinning model. Appl Phys Lett. doi:10.1063/1.2911735

[54] Zhu YT, Liao XZ, Wu XL (2008) Deformation twinning in bulk nanocrystalline metals: experimental observations. JOM 60:60–64. doi:10.1007/s11837-008-0120-1

[55] Legros M, Hemker KJ, Gouldstone A, Suresh S, Keller-Flaig RM, Arzt E (2002) Microstructural evolution in passivated al films on si substrates during thermal cycling. Acta Mater 50:3435–3452. doi:10.1016/s1359-6454(02)00157-x

[56] Miyazawa K, Iwasaki Y, Ito K, Ishida Y (1996) Combination rule of sigma values at triple junctions in cubic polycrystals. Acta Crystallogr Sect A 52:787–796. doi:10.1107/s0108767396005934

[57] Thompson CV (2000) Structure evolution during processing of polycrystalline films. Annu Rev Mater Sci 30:159–190. doi:10.1146/annurev.matsci.30.1.159

[58] Olmsted DL, Foiles SM, Holm EA (2009) Survey of computed grain boundary properties in face-centered cubic metals: I. Grain boundary energy. Acta Mater 57:3694–3703. doi:10.1016/j.actamat.2009.04.007

[59] Nix WD (2014) Metallic thin films: stresses and mechanical properties. In: Barmak K, Coffey KR (eds) Metallic films for electronic, optical and magnetic applications. Woodhead Publishing, Cambridge